Chapter 8

Imaging subducted slab structure beneath the Sea of Okhotsk with teleseismic waveforms

8.1 Introduction

Seismic images have revealed a complicated fate of subducted slabs, including penetrating into the lower mantle, stagnating in the transition zone, flat subducting and tearing. Approaches to derive these slab images are based mostly on travel times, and have evolved in the last decades with increasing data sets and progress in methodology (see Lay (1994) for a review). In the 1960s and 70s, teleseismic P-wave travel-times from shallow nuclear explosions and earthquakes suggested the existence of subducted slabs as dipping high-velocity layers (e.g., Davies and Julian, 1972; Sleep, 1973). To test the hypothesis of whole-mantle convection, numerous studies applied the residual sphere method to teleseismic travel times from deep earthquakes, and found high-velocity (3-5%) slabs penetrating into the lower mantle in most of the west and northwest Pacific subduction zones (e.g., Jordan, 1977; Creager and Jordan, 1984, 1986; Fischer et al., 1988; Fischer et al., 1991). To avoid biases from lower-mantle and station-side structures (e.g., Zhou et al., 1990; Ding and Grand, 1994) applied the residual sphere method to differential travel times from shallow and deep earthquakes in the Kuril subduction zone. They reported high-velocity (~5%) slab in the upper mantle, but complicated structure in the lower mantle. From the 1990s, with increasing quantity and quality of seismic data, global and regional travel-time tomography has been providing increasingly detailed images of subducted slabs (e.g., Zhou, 1990; van der Hilst et al., 1991; Zhao et al., 1992; Li et al., 2008; Simmons et al., 2012). Tomography models show that subducted slabs could have complex morphology (e.g., flat subduction, tearing), and could penetrate into the lower mantle or become stagnant in the transition zone. However, resolution of tomography is limited by data coverage, damping and accuracy of earthquake locations. For example, in most tomography models, the velocity perturbations of slabs are on the order of 1%, much smaller than the earlier results (~5%) from travel-time modeling mentioned above or waveform modeling discussed in this paper.

Seismic waveforms have better sensitivities to velocity perturbations and sharpness than travel time alone. For example, Silver and Chan (1986) observed multipathing of teleseismic S waves from deep earthquakes beneath the Sea of Okhotsk, and explained them as evidence for slab extension in lower mantle. Using the Cagniard-de Hoop method, Mellman and Helmberger (1974) demonstrated that a thin high-velocity layer has similar effect as attenuation (elastic-wave tunneling effect). Vidale (1987) coupled 2D finite-difference method near the source with Kirchhoff method in the far field, and predicted waveform broadening at take-off angles sub-parallel with the slab. This broadening was confirmed latter by Cormier (1989) using the Gaussian beam theory. However, these predicted teleseismic waveform effects from earthquakes close to or within subducted slab have not been systematically tested due to the sparse global networks at that time (e.g., Vidale and Garcia-Gonzalez, 1988; Cormier, 1989). Furthermore, Beck and Lay (1986) and Cormier (1989) pointed out another major difficulty with teleseismic waveform modeling that other deep-mantle heterogeneities or station-side structures could cause similar waveform distortions as subducted slabs.

In this paper, we demonstrate that the difficulties with slab waveform modeling can be overcome given the much denser global network and the better numerical methods now available. In particular, with examples in the Kuril subduction zone, we find that the P wave velocity in the slab center is about 5% higher than the ambient mantle, and we also test the waveform sensitivity to slab sharpness and depth extension of subducted oceanic crust.

Before going to the details of our teleseismic waveform modeling, we wish to acknowledge that waveform modeling of slab has been performed in subduction zones with regional networks (e.g., Abers, 2000; Chen et al., 2007; Savage, 2012). For example, by modeling two deep earthquakes' up-going waveforms recorded by Hi-Net, Chen et al. (2007) refined the slab model beneath Japan with about 4.5% high-velocity in the slab, and an elongated strong low-velocity layer on top to large depth. However, for many subduction zones without dense regional networks (e.g., Kuril), the teleseismic waveform modeling is still sufficient to refine slab models.

In the following, we first introduce the waveform effects of a high-velocity slab using our 2D finite-difference method. Then, we analyze the teleseismic waveforms from two earthquakes in the Kuril subduction zone and invert for slab velocity perturbation and sharpness.

8.2 Waveform effects of a high-velocity slab

The waveform effects of a high-velocity slab have been studied by different methods. In this paper, we use an efficient GPU-based 2D finite-difference (FD) method to simulate the full global wavefield with a high-velocity slab (Li et al., 2013). It takes only about 30 minutes to simulate the teleseismic wavefield to 1 Hz with 2 GPUs. This fast speed allows the testing of many different kinds of slab models efficiently. In the following we will demonstrate slab's waveform effects with four examples of high-velocity slab within homogeneous background.

The first example model consists of a homogeneous background with Vp=8 km/s, and a 60 km thick, 500 km long slab (the black solid rectangle in Figure 8.1A) with uniform velocity perturbation of 3%. An isotropic explosion source is placed in the left end of the slab (the red star in Figure 8.1A). The snapshot of the velocity field shows distorted P waves along directions sub-parallel with the slab, outlined by the wedge between the two red lines. In the right panel of Figure 8.1A, we plot the synthetic P waveforms at a line of stations (small triangles in left panel of Figure 8.1A) and align them on the theoretical travel times without the high-velocity slab. Waves arriving before the theoretical travel times (filled with red) have been speed up by the slab, and display waveform complexities (double arrivals). The first arrivals travel along the slab, and the second broader arrivals diffract around the slab (Vidale, 1987). Based on geometrical ray theory, the angular range of distorted waveforms can be approximated by $\sin(\frac{\pi}{2} - \theta) \approx \frac{1}{1+\delta}$, where θ is the angle between the red lines and slab in Figure 8.1A, δ is the velocity perturbation of the slab. Therefore, larger velocity perturbation δ causes wider range of waveform distortion (large θ angle), which is confirmed by our second example in Figure 8.1B with increased slab velocity perturbation (6%). On the other hand, sharpness of slab controls the waveform shapes. In Figure 8.1C, we set a triangular velocity profile across the slab with the highest perturbation in the slab center (6%), and drops in constant gradient to the background velocity on both edges. The average velocity perturbation is 3%, similar to the first example in Figure 8.1A. The simulated waveforms display distortions within similar range as in Figure 8.1A, but are smoother without double pulses. This is because the waves traveling along or diffracted around the slab are not as distinct as in Figure 8.1A. In Figure 8.1D, slab with triangular velocity profile and 12% perturbation in the center produces smooth waveforms as in Figure 8.1C, but wide range of distortions as in Figure 8.1B due to the similar average perturbation.

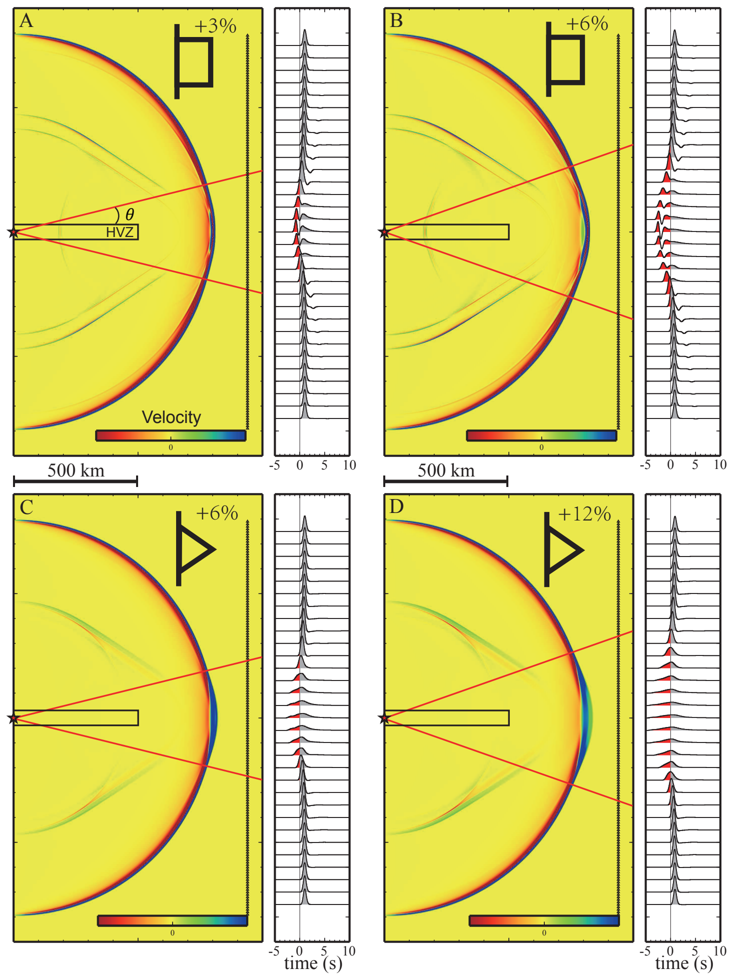

Figure 8.1: Examples of waveform complexity caused by a high-velocity slab. The finite-difference simulations of the full wavefield from an explosion source (star) at the left end of various high velocity slabs (black rectangle) are displayed assuming a grid-size of 1 km. In (A), the velocity profile across the slab is uniformly 3% higher than the homogeneous ambient material (Vp=8 km/s) as shown by the inset. The background shows a snapshot of the velocity wavefield with strong P waves and weak P-to-S converted phases from slab edges. The right panel displays the synthetic seismograms recorded on the linear array (small triangles) in the right part of the model. The seismograms are aligned by predicted travel times without the slab, and the earlier arrivals are filled by the red color. The wedge defined by the two red lines displays the range of stations with waveform distortions. (B) Similar to (A) but with a 6% uniform velocity perturbation within the slab. (C) Similar to (A) but with triangular velocity profile across the slab as shown by the inset. (D) Similar to (C) but with a 12% velocity perturbation in the slab core.

In summary, the four examples demonstrate consistent waveform effects of slab as in previous studies (e.g., Vidale, 1987). In particular, we find that slab sharpness and perturbation control the waveform shapes and the angular range of distortions, respectively. In the next section, we will present similar phenomena observed for earthquakes close to or within subducted slabs, and model slab velocity perturbations and sharpness.

8.3 Data

Our study region is the middle section of the Kuril subduction zone (Figure 8.2A). In this area, the relocated EHB catalog (Engdahl et al., 1998) shows that seismicity continues down to ~600 km depth, and has relatively little variation along strike (Figure 8.2B). Therefore, the slab structure is close to a 2D problem along the down-dip direction, suitable for 2D waveform modeling (thick black line in Figure 8.2A). We study two earthquakes (red beachballs in Figure 8.2A), one on each side of the Kuril trench. The 2009/09/10, Mw5.9 earthquake is a shallow-angle thrust event at a depth of 37 km located on the plate interface, while the 2007/01/13 Mw6.0 earthquake is a shallow outer-rise event. Both earthquakes have relatively simple source processes without obvious directivity. Figure 8.3A shows the teleseismic P wave record-section of the 2009 interplate earthquake within 45° of the downdip azimuth (315°), aligned by the hand-picked P onsets. While the P and sP pulses have durations of ~2s at distances larger than 65°, the waveforms are significantly broader at distances less than 65°. The transition from narrow to broad pulses occurs between 70° and 60°, which correspond to only a ~3° difference in the take-off angles. Therefore, the observed distance-dependence of waveforms is too sharp to be explained by any source directivity, but requires structural anomalies near the source or in the deep mantle. Station-side structures are less likely because stations with similar distances record

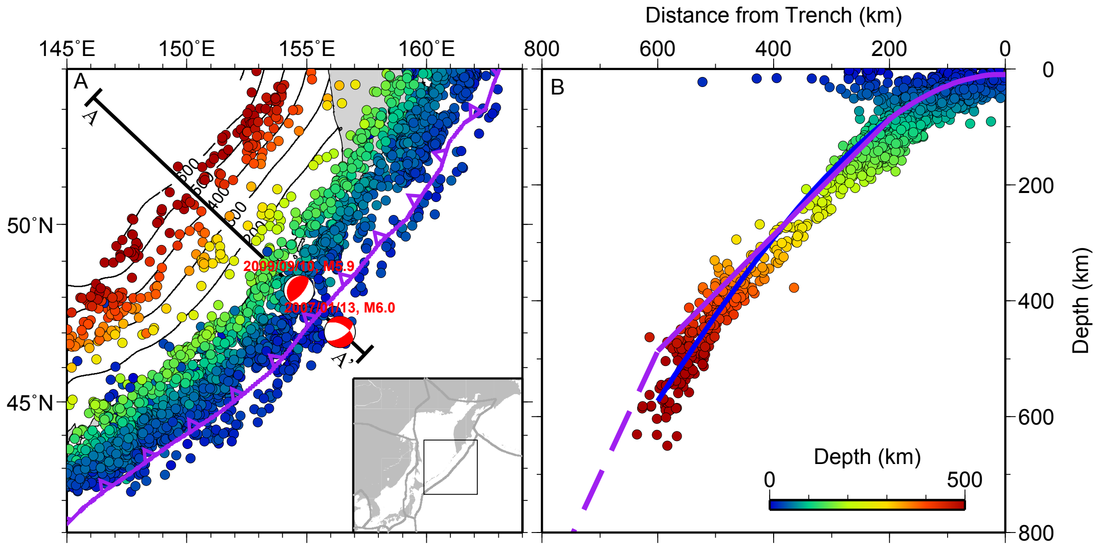

Figure 8.2: (A) Map and relocated seismicity of the Kuril subduction zone. Box in the inset shows the location of our study area. The dots are the earthquakes in the EHB catalog from 1961 to 2008, colored by their depths. The slab depth contours are from Slab 1.0 (Hayes et al., 2010). The two red beachballs show the two earthquakes studied in this paper, one on each side of the trench (purple barbed line). AA' displays the location of cross-sections in Figure 8.3. (B) Plot of seismicity versus distance from trench and depth. The thick blue line is the slab geometry from the Slab 1.0, while the purple line is the modified geometry used in this paper. The dashed purple line shows the lower mantle slab extension tested in this paper.

similar waveform broadenings even though they are far apart in locations. On contrary, similar P record-section for the nearby 2007 outer-rise earthquake (Figure 8.3B) does not show any waveform broadening, even though it samples almost the same lower-mantle and station-side structures. Therefore, we conclude that the observed waveform broadening of the 2009 earthquake is caused by near-source structures.

The major differences in the ray paths between the 2007 and the 2009 earthquakes are whether they sample the subducted slab. Here we use a slab geometry constrained by the relocated seismicity to illustrate this point. Hayes et al. (2012) obtained a smooth slab model for this region (Slab 1.0), as shown by the thick blue line in Figure 8.2B. Note that at depths larger than 400 km, the slab geometry fits through the middle of the deep seismicity. Since deep earthquakes occur in the cold core

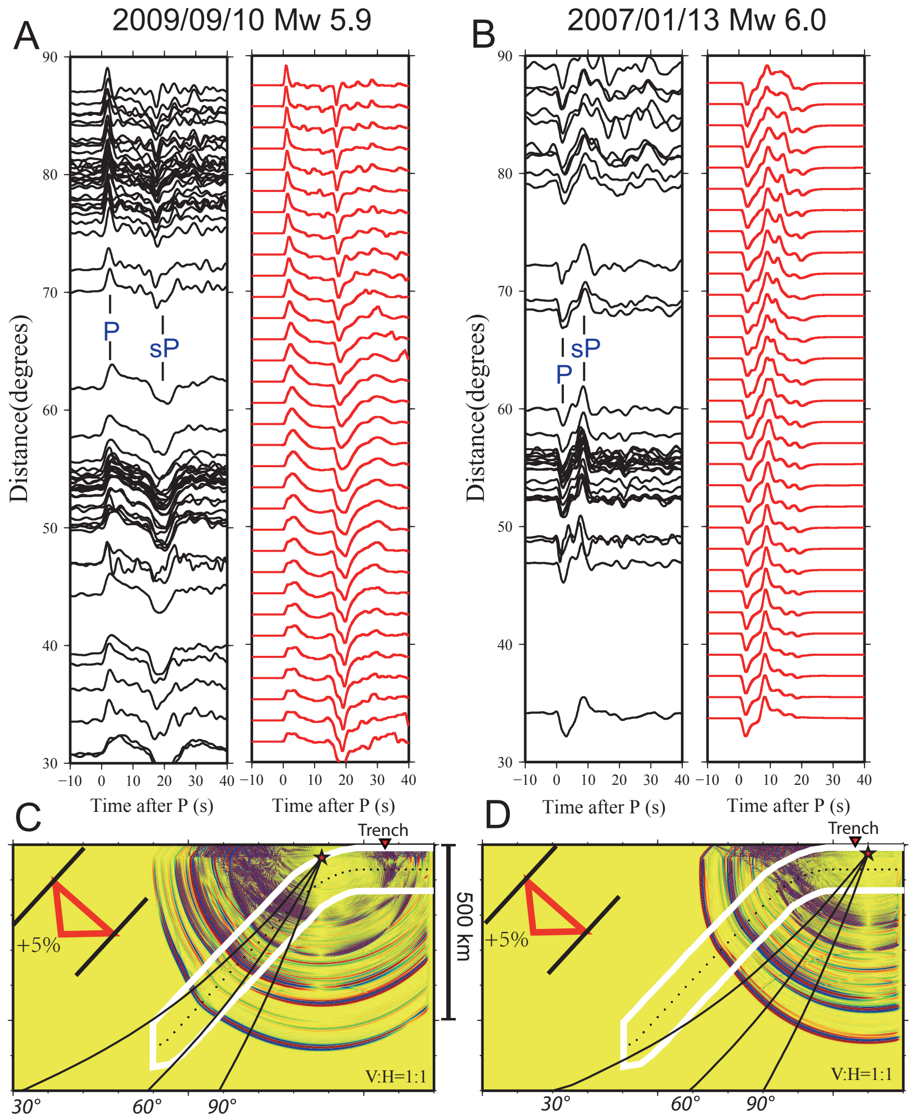

Figure 8.3: Waveform observations and simulations for the 2009/09/10 Mw5.9 interplate earthquake and the 2007/01/13 Mw6.0 outer-rise earthquake. (A) Distance record-sections of observed (left panel, black) and synthetic (right panel, red) seismograms for the 2009 interplate earthquake, aligned by the first P arrivals. (B) Similar to (A) but for the 2007 outer-rise earthquake. Figure 8.4 shows the comparisons of observed and synthetic full waveforms. (C) 2D finite-difference simulation of the 2009 interplate earthquake (red star) with a high-velocity slab (outlined by the white line). The inset shows the triangular velocity profile across the slab, with 5% perturbation in the slab center. Black lines display the P wave ray paths to teleseismic distances of 30°, 60° and 90°, respectively. (D) Similar to (C) but for the 2007 outer-rise earthquake.

of subducted slabs, we modify the slab geometry to fit the top of the seismicity (thick purple line in Figure 8.2B). Given the modified slab geometry, we outline the subducted slab as white lines in a vertical cross-section (Figure 8.3C and 8.3D) along line AA' in Figure 8.2A. As shown in Figure 8.3D, the 2007 outer-rise earthquake (red star) occurred to the east of the trench, and its teleseismic ray paths to 30°, 60° and 90° have little interaction with the subducted slab. In contrast, teleseismic ray paths of the 2009 interplate earthquake travel along the slab to 30° and 60°, but avoid the slab at larger ranges (90°) (Figure 8.3C). This dependence of slab sampling with take-off angles coincides with the observed distance-dependent waveform broadening, and is very similar to the synthetic examples shown in Figure 8.1. Therefore, we conclude that the observed waveform broadening of the 2009 earthquake is caused by the subducted slab structure. In the next section, we will invert the observed waveform broadening for slab perturbation and sharpness in the 2D vertical cross-section along line AA' in Figure 8.2A.

8.4 Slab velocity model

8.4.1 Velocity perturbation

The synthetic examples in Figure 8.1 demonstrate that velocity perturbation controls the transition from simple to distorted waveforms. Similarly, the observed transition around 65° for the 2009 interplate earthquake is also sensitive to slab velocity perturbations. Here we search for the best-fitting models by testing a variety of slab thickness-perturbation-sharpness combinations, using the fast GPU-based 2D FD method. We simulate the full global wavefield with PREM as the background model. Our preferred slab model has a triangular velocity profile across a 120km thick slab, with a maximum perturbation of 5% in the slab core (insets in Figure 8.3C and 8.3D). The velocity snapshots of the simulated wavefields (colored back-

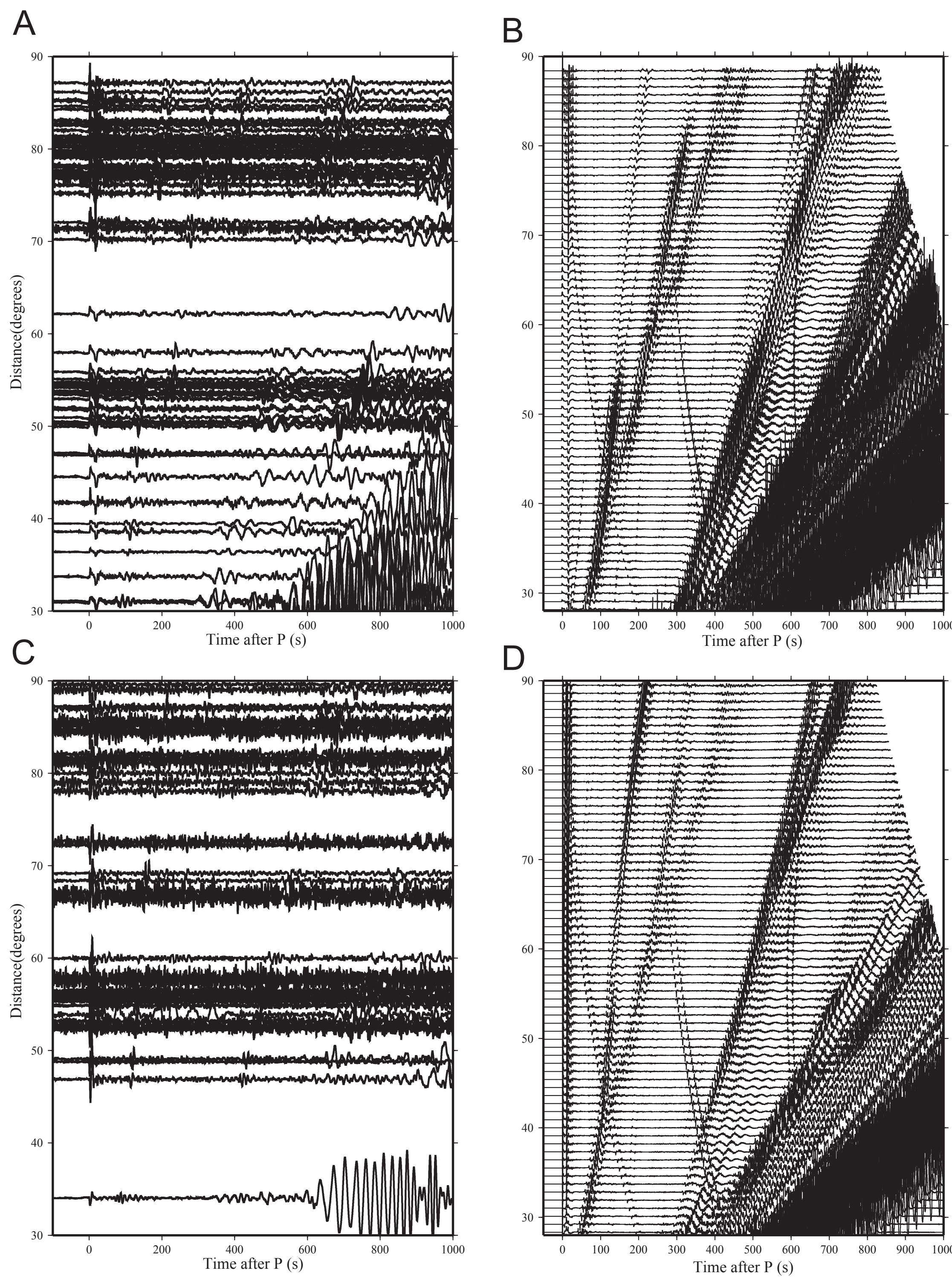

Figure 8.4: Complete record sections of the 2009 and 2007 earthquakes. (A) and (B) are the data and synthetics for the 2009 interplate earthquake, respectively. (C) and (D) are the data and synthetics for the 2007 outer-rise earthquake, respectively.

grounds in Figure 8.3C and 8.3D) show obvious speed-up of the wavefronts occurs along the slab. The synthetic seismograms for the 2009 interplate earthquake plotted side-by-side with the observations in Figure 8.3A reproduce the sharp transition from simple to broad waveforms between 70° and 60°. With the same slab model, the synthetics for the 2007 outer-rise event do not have any waveform distortion due to the slab, consistent with the observed waveforms (Figure 8.3B). Note that the 5% perturbation is significantly higher than previous travel-time tomography results for this region (~1%, e.g., Li et al., 2008; Simmons et al., 2012).

8.4.2 Slab sharpness

After explaining the transition from simple to broad waveforms around 65° distance, we turn to the waveform details to constrain the slab sharpness. As a reference, we show the waveform fitting for the preferred model with triangular velocity profile in Figure 8.5A. On tops of Figure 8.5B and 8.5C, we modify the velocity profile across the slab to have either sharp edges on both sides, or only sharp top but smooth bottom. The synthetic seismograms for each case are compared with the observations. In Figure 8.5B, the sharp edges on both sides produce distinct early arrivals (marked by the blue dashed line), which are not observed in real data. These distinct arrivals due to the sharp slab are similar to the double pulses in the synthetic examples in Figure 8.1A and 8.1B. The slab model with only sharp top (Figure 8.5C) provides similar waveform fitting as the preferred model, therefore we cannot distinguish the models in Figure 8.5A and 8.5C using the current dataset.

8.4.3 Low-velocity oceanic crust

How far does the low-velocity oceanic crust persist into the mantle is another major question for slab structures. As reviewed by Bostock (2012), the low-velocity zone (LVZ) starts to fade in seismic images between 40 km and 120 km, depending on

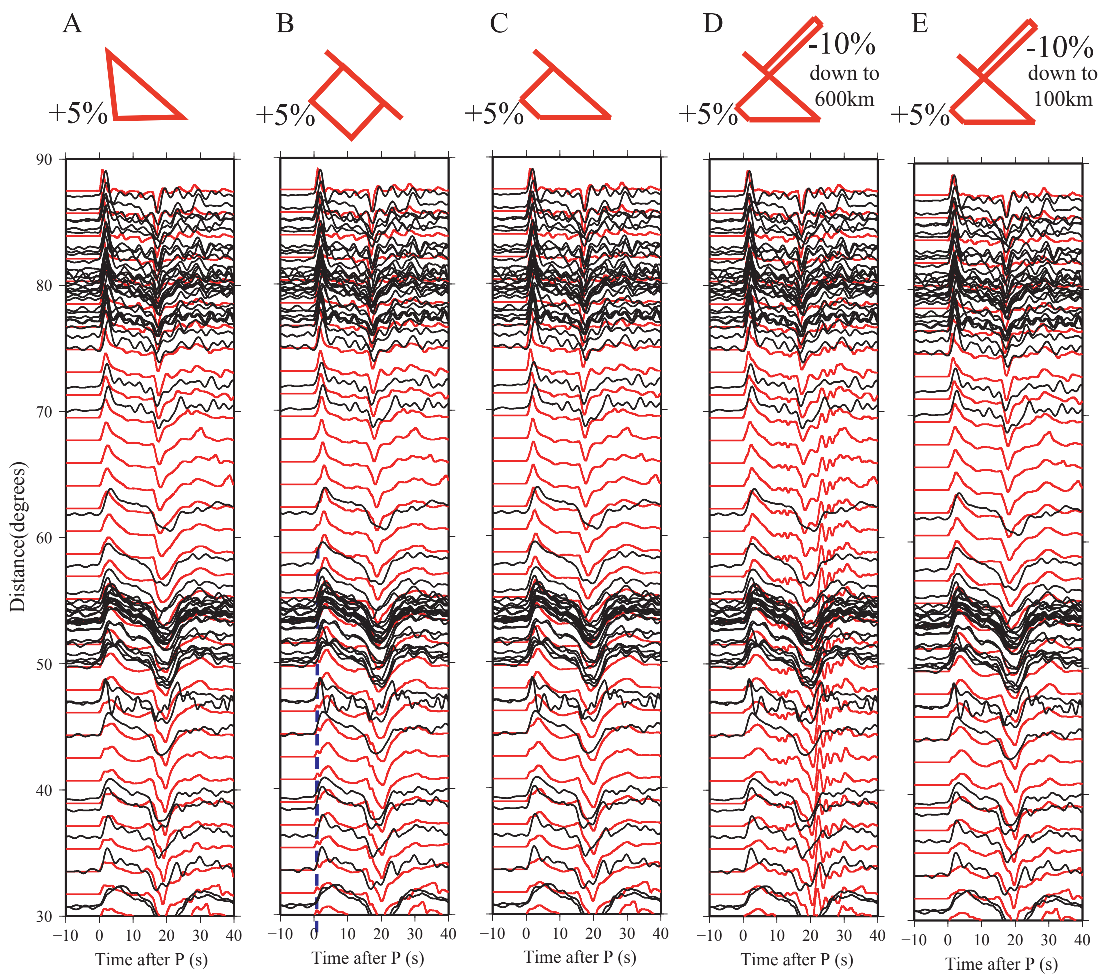

Figure 8.5: Tests of waveform sensitivities to slab sharpness. For each panel, the observed seismograms are shown as black, and the synthetics using different velocity profiles across the slab (displayed on top) are in red. (A) has smooth edge on each side, (B) has sharp edges on both sides, (C) has sharp top but smooth bottom. (D) and (E) are modified from (C) with a low-velocity layer on top, to 600 km and 100 km, respectively.

the thermal states. This fading is usually associated with the basalt-to-eclogite transition. However, there are also examples in which the LVZ persists to much larger depths (e.g., Abers, 2000; Chen et al., 2007). Here for the Kuril subduction zone, we test the teleseismic waveform sensitivity to the depth extent of LVZ using two end-member models, one with a 10 km thick, -10% LVZ down to 600 km depth, another with the same LVZ but only to 100 km depth, as shown in Figure 8.5D and 8.5E, respectively. In Figure 8.5D, the long LVZ serves as a strong wave-guide and produces strong high-frequency teleseismic coda waves in the synthetics, which are not observed in the real data. On contrary, the synthetics with LVZ down to 100 km fit the observations better (Figure 8.5E). Therefore, it is unlikely to have a coherent LVZ down to large depth beneath the Sea of Okhotsk, consistent with the basalt-to-eclogite transition. However, we cannot rule out a low-velocity layer to large depth with irregular geometries or strong scatterers inside to break the wave-guide effect (e.g., Savage, 2012).

8.4.4 Depth sensitivity and slab extension in the lower mantle

Due to limited depth resolution using only shallow earthquakes, in the models above we assume that the slab structure is uniform along the length direction and truncate the slab at depth of 600 km. However, we believe this approximation does not significantly affect the results in this paper because the thermally controlled velocity structure varies slowly along the slab. We also test models with high-velocity slab extension into the lower mantle (dashed purple line in Figure 8.2B) and find little difference in data fitting. Waveform modeling of earthquakes at different depths will provide better depth sensitivity to resolve any sharp velocity variations along the slab length direction due to phase changes. In particular, to separate the effects from the upper- and lower-mantle slab, we will need to model waveforms from deep earthquakes near the 660 km discontinuity. With the global full-wavefield simulation method, our waveform modeling approach applies to earthquakes at all depths.

8.5 Conclusion and future work

In this paper, we have studied the teleseismic P waveforms from two shallow earthquakes in the Kuril subduction zone to constrain the subducted slab structures. We observed strong distance-dependent waveform broadening and inverted for a high-velocity subducted slab with a triangular velocity profile. The maximum velocity perturbation in the slab core is 5%, significantly higher than most previous travel-time tomography models for this region (Li et al., 2008; Simmons et al., 2012), but consistent with earlier results from residual sphere method (Ding and Grand, 1994). We rule out slab models with both sharp top and bottom, suggesting that the slab structure is thermally controlled to the first order. The data also rejects a coherent low-velocity layer down to large depth, consistent with the model of basalt-to-eclogite transition at about 100 km depth (Bostock, 2012).

As pointed out by earlier investigators, teleseismic waveforms from subduction zone earthquakes have great potential in determining better images of subducted slabs, especially for areas without dense regional network. However, teleseismic waveform modeling has ambiguities with deep-mantle heterogeneities or station-side structures. In this paper, we have shown that we can overcome this ambiguity with the dense global seismic network and fast numerical methods. To resolve more details of slab structure, such as variations along the length direction and lower mantle slab extension, we need to include more earthquakes at different depths. Furthermore, since we use a full wavefield method, we can include many other teleseismic phases (e.g., PcP, PP, S, ScS, SS, see Figure 8.6) which have different sensitivities to the slab structures. 3D waveform modeling could incorporate more data off the downdip azimuth, but requires a lot more computational power in simulations of global wavefield to 1 Hz. One possible solution would be hybrid methods which couple expensive 3D methods near the source region and cheaper 1D approaches in the far field (e.g., Zhan et al., 2012).

References

Abers, G.A., 2000. Hydrated subducted crust at 100-250 km depth. Earth Planet Sc Lett 176, 323-330.

Beck, S.L., Lay, T., 1986. Test of the Lower Mantle Slab Penetration Hypothesis Using Broad-Band S-Waves. Geophys Res Lett 13, 1007-1010.

Bostock, M., 2012. The Moho in subduction zones. Tectonophysics in press.

Chen, M., Tromp, J., Helmberger, D., Kanamori, H., 2007. Waveform modeling of the slab beneath Japan. Journal of Geophysical Research 112.

Cormier, V.F., 1989. Slab Diffraction of S-Waves. Journal of Geophysical Research 94, 3006-3024.

Creager, K.C., Jordan, T.H., 1984. Slab Penetration into the Lower Mantle. Journal of Geophysical Research 89, 3031-3049.

Creager, K.C., Jordan, T.H., 1986. Slab Penetration into the Lower Mantle beneath the Mariana and Other Island Arcs of the Northwest Pacific. Journal of Geophysical Research 91, 3573-&.

Davies, D., Julian, B.R., 1972. A Study of Short Period P-wave Signals from Longshot. Geophysical Journal of the Royal Astronomical Society 29, 185-202.

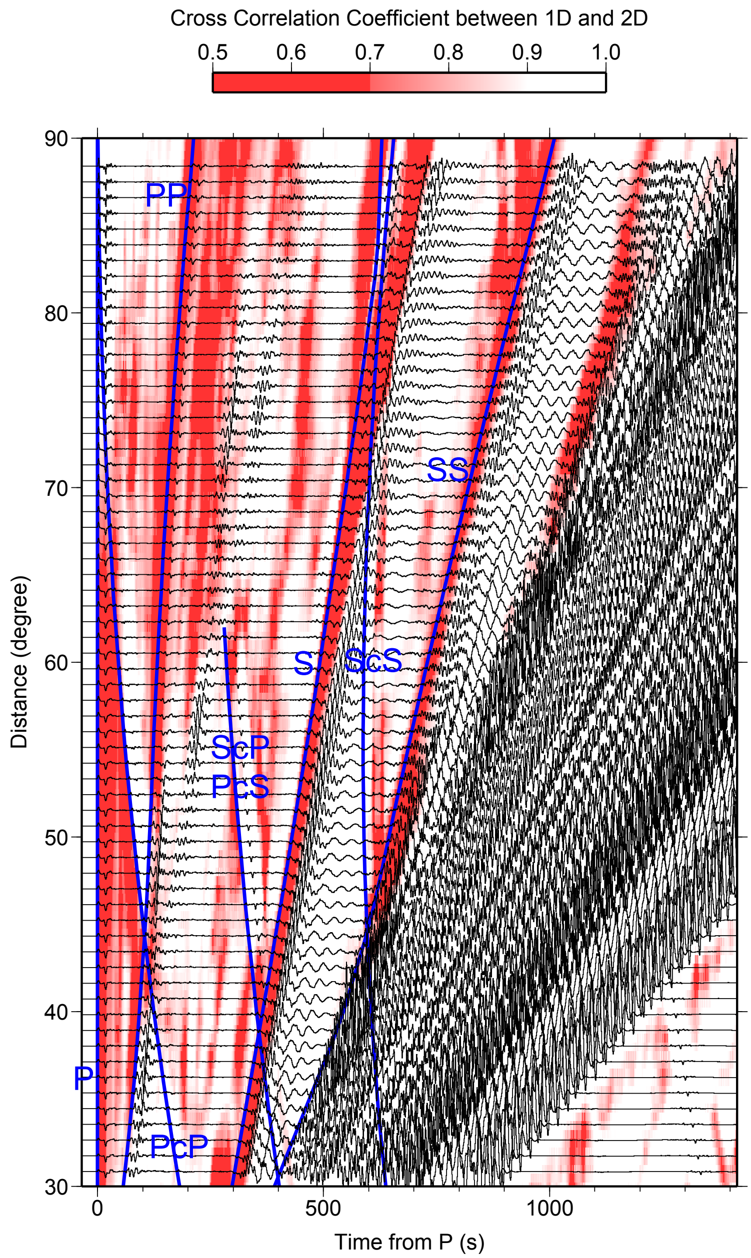

Figure 8.6: Complete synthetic record section of the 2009 earthquake with the preferred slab model. The blue lines mark the major teleseismic body wave phases. The wave packages with largest amplitudes are the surface waves. To high-light the effect of the subducted slab, we compare the synthetic seismograms from models with/without the slab by cross-correlation. The background color shows the maximum cross-correlation coefficients allowing 5s shift. High cross-correlation (>0.9, white) means little waveform effect from slab, and low cross-correlation (<0.7, red color) highlights strongly distorted waveforms. Note that the surface waves with large amplitudes are not affected by the slab structure.

Ding, X.Y., Grand, S.P., 1994. Seismic Structure of the Deep Kurile Subduction Zone. Journal of Geophysical Research 99, 23767-23786.

Engdahl, E.R., van der Hilst, R., Buland, R., 1998. Global teleseismic earthquake relocation with improved travel times and procedures for depth determination. B Seismol Soc Am 88, 722-743.

Fischer, K.M., Creager, K.C., Jordan, T.H., 1991. Mapping the Tonga Slab. Journal of Geophysical Research 96, 14403-14427.

Fischer, K.M., Jordan, T.H., Creager, K.C., 1988. Seismic Constraints on the Morphology of Deep Slabs. Journal of Geophysical Research 93, 4773-4783.

Hayes, G.P., Wald, D.J., Johnson, R.L., 2012. Slab1. 0: A three-dimensional model of global subduction zone geometries. Journal of Geophysical Research 117.

Jordan, T., 1977. Lithospheric slab penetration into the lower mantle beneath the Sea of Okhotsk. J. Geophys 43, l977.

Lay, T., 1994. The Fate of Descending Slabs. Annu Rev Earth Pl Sc 22, 33-61.

Li, C., van der Hilst, R.D., Engdahl, E.R., Burdick, S., 2008. A new global model for P wave speed variations in Earth's mantle. Geochemistry, Geophysics, Geosystems 9.

Li, D., Helmberger, D., Clayton, R., and Sun, D., 2013. Global synthetic seismograms using 2D Finite Difference, Geophysical Journal International, submitted.

Mellman, G.R., Helmberger, D.V., 1974. High-frequency attenuation by a thin high-velocity layer. B Seismol Soc Am 64, 1383-1388.

Savage, B., 2012. Seismic constraints on the water flux delivered to the deep Earth by subduction. Geology 40, 235-238.

Silver, P.G., Chan, W.W., 1986. Observations of body wave multipathing from broadband seismograms: Evidence for lower mantle slab penetration beneath the Sea of Okhotsk. Journal of Geophysical Research 91, 13787-13713,13802.

Simmons, N.A., Myers, S.C., Johannesson, G., Matzel, E., 2012. LLNL-G3Dv3: Global P wave tomography model for improved regional and teleseismic travel time prediction. Journal of Geophysical Research 117.

Sleep, N.H., 1973. Teleseismic P-Wave Transmission through Slabs. B Seismol Soc Am 63, 1349-1373.

van der Hilst, R., Engdahl, E., Spakman, W., Nolet, G., 1991. Tomographic imaging of subducted lithosphere below northwest Pacific island arcs. Nature 353, 37-42.

Vidale, J.E., 1987. Waveform effects of a high-velocity, subducted slab. Geophys Res Lett 14, 542-545.

Vidale, J.E., Garcia-Gonzalez, D., 1988. Seismic observation of a high-velocity slab 1200–1600 km in depth. Geophys Res Lett 15, 369-372.

Zhan, Z., Helmberger, D., Simons, M., Kanamori, H., Wu, W., Cubas, N., Duputel, Z., Chu, R., Tsai, V.C., Avouac, J.-P., 2012. Anomalously steep dips of earthquakes in the 2011 Tohoku-Oki source region and possible explanations. Earth Planet Sc Lett 353, 121-133.

Zhao, D.P., Hasegawa, A., Horiuchi, S., 1992. Tomographic Imaging of P-Wave and S-Wave Velocity Structure beneath Northeastern Japan. Journal of Geophysical Research 97, 19909-19928.

Zhou, H.-W., Anderson, D.L., Clayton, R.W., 1990. Modeling of residual spheres for subduction zone earthquakes: 1. Apparent slab penetration signatures in the NW

Pacific caused by deep diffuse mantle anomalies. Journal of Geophysical Research 95, 6799-6827.

Zhou, H.W., 1990. Mapping of P-Wave Slab Anomalies beneath the Tonga, Kermadec and New Hebrides Arcs. Phys Earth Planet In 61, 199-229.